NUCL SCI TECH (2022) 33:79
https://doi.org/10.1007/s41365-022-01053-7

Spherical nanoindentation stress–strain responses of SIMP steel to synergistic effects of irradiation by H and He ions

Peng Jin[1,2] · Tie-Long Shen[1,2] · Jing Li[1,2] · Yu-Shan Yang[1,2] · Jian-Long Chai[1,2] · Ya-Bin Zhu[1,2] · Ming-Huan Cui[1,2] · Chao Liu[1,2] · Tong-Min Zhang[1] · Long Kang[1] · Jun Li[1] · Jin-Yu Li[1] · Shuo-Xue Jin[3] · Xing-Zhong Cao[3] · Zhi-Guang Wang[1,2]

Received: 18 November 2021 / Revised: 22 March 2022 / Accepted: 28 April 2022 / Published online: 9 July 2022

Abstract A novel Fe-10Cr ferritic/martensitic steel called SIMP was chosen to investigate synergistic effects of H and He on the mechanical properties of structural materials for innovative nuclear energy systems. Sequential and separate irradiation experiments on SIMP steel specimens at room temperature using H and He ions with various energy levels were conducted to produce an ion deposition plateau at 300–650 nm. The indentation stress–strain responses were examined using spherical nanoindentation tests after the irradiation experiments. It was found that the sequential irradiation by He and H produced a higher indentation yield stress than separate irradiation, indicating that the hardening was enhanced by the synergy of the H and He irradiation. The micro-mechanism responsible for enhancing the hardening of the SIMP steel through the H and He synergy was investigated using Doppler broadening spectroscopy detection and transmission electron spectroscopy observations.

Keywords H/He irradiation · Spherical nanoindentation · Bubbles · Dislocation loops

1 Introduction

The simultaneous production of significant amounts of H and He might have serious effects on the mechanical performances of structural materials in nuclear energy systems, especially in fusion reactors and spallation target environments [1–3]. It has been demonstrated experimentally that the irradiation swelling can be enhanced by a H/He synergistic effect in Fe–Cr alloys and steels [4, 5]. This is thought to be related to the gas pressures of the H and He in cavities during the irradiation [5]. Based on atomistic simulations, Hayward and Deo further pointed out that H can assist He bubbles to grow by enhancing "loop punching" [6], providing a probable explanation for this H/He synergistic effect. In addition to the swelling, the enhancement of irradiation hardening by the H/He synergistic effect has also been reported for some steels [7–9]. However, there is still limited information available about the H/He synergistic effects on the mechanical properties of structural materials, and the micro-mechanism responsible.

Beam irradiation using multiple ions (including H and He ions) has commonly been used to simulate the synergy environment of H and He in materials [1, 4, 5]. Nevertheless, only a shallow irradiated layer can be formed by ion irradiation, which makes it difficult to measure the changes in the mechanical properties induced by ion

This work was supported by the National Natural Science Foundation of China under grants (Nos. U1832206, 11505246, 11605256, 91426301, 11405231, 11575258, 11375242, and 11505247) and the key projects of the Chinese Academy of Sciences (No. ZDRW-CN-2017-1).

✉ Tie-Long Shen
shentielong@impcas.ac.cn

✉ Zhi-Guang Wang
zhgwang@impcas.ac.cn

1 Institute of Modern Physics, Chinese Academy of Sciences, Lanzhou 730000, China

2 School of Nuclear Science and Technology, University of Chinese Academy of Sciences, Beijing 100049, China

3 Institute of High Energy Physics, Chinese Academy of Sciences, Beijing 100049, China

irradiation using conventional mechanical tests. Instead, nanoindentation has been widely adopted because of its potential to extract local information from a shallow layer at the nanoscale and advantage of using a small specimen for testing [10, 11]. In previous studies, hardness and modulus measurements were normally performed using a Berkovich indenter [7–9, 12]. However, it is unsuitable for estimating the yield strength or elastic–plastic transition. In contrast, a spherical indenter is considered to be a powerful tool for determining these properties using indentation stress–strain curves [13–15]. In particular, with the development of the protocol for spherical nanoindentation [13, 16], it has exhibited great potential for studying the mechanical property changes in materials caused by ion irradiation [17–20].

SIMP steel is a novel ferritic/martensitic (F/M) steel with a good balance of heat, radiation, and corrosion resistances. It is therefore expected to be used as a structural material for the spallation target of an accelerator-driven subcritical system (ADS) in the future [21]. In the present study, SIMP steel was used to study the mechanical response of a structural material to the synergistic effects of H and He irradiation using spherical nanoindentation. The intrinsic mechanism of the changes was also investigated.

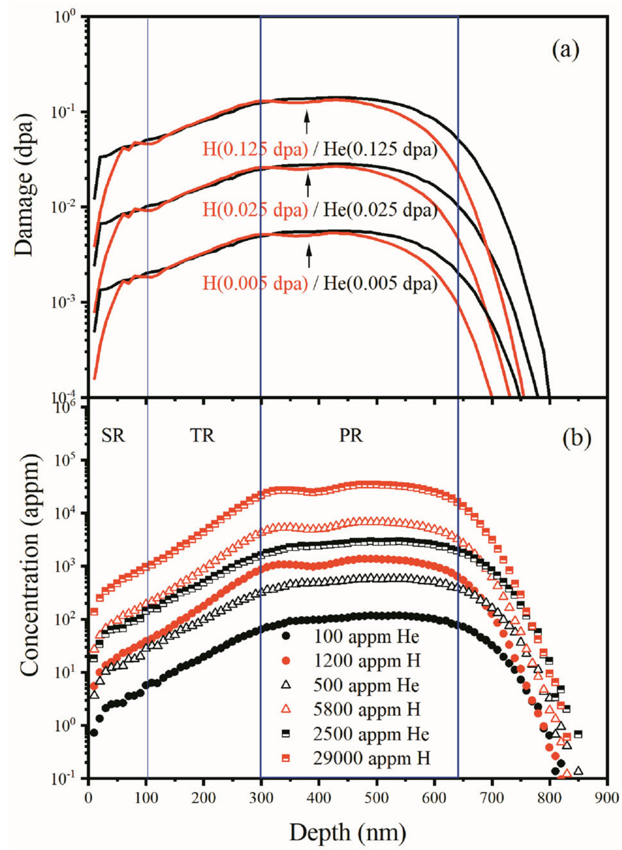

Fig. 1 (Color online) Depth profiles of **a** damage level and **b** H/He concentration in SIMP steel irradiated by He and/or H ions with multiple energy levels, according to SRIM 2013 calculations. An ion deposition plateau was produced at approximately 300–650 nm

2 Materials and methods

2.1 Materials

The detailed development process for SIMP steel can be found in a reference [21]. The as-received steel samples were normalized for 0.5 h at (1040 ± 10) °C and tempered for 1.5 h at (760 ± 10) °C [21]. Their chemical composition (wt%, with Fe making up the balance) included Cr (10.24), Si (1.22), C (0.22), Mn (0.52), W (1.45), Ta (0.12), V (0.18), S (0.004), and P (0.004). The SIMP samples had a cross-section of approximately 7 × 15 mm^2. They were ground and polished to form a suitable surface for irradiation, and then annealed for 1 h at 600 °C in a vacuum at better than 1 × 10^{-4} Pa to remove the work hardening surface layer and prevent it from influencing the subsequent nanoindentation test.

2.2 Irradiation experiments

Irradiation experiments were carried out at the 320 kV multi-discipline research platform for highly charged ions at the Institute of Modern Physics (IMP) in Lanzhou, China. Two irradiation modes were adopted for comparison, one was the sequential irradiation of He and H (He + H), and the other was the separate irradiation of He and H. Based on SRIM 2013 calculations in the "quick Kinchin-Pease calculation" mode [22, 23], 100–250 keV He^+ and 60–130 keV H^+ were chosen to produce an ion deposition plateau (PR) at 300–650 nm (Fig. 1). In Fig. 1, SR represents the surface region, which was easily influenced by surface treatment. TR refers to the track region [24]. In the SRIM calculations, the density of the target material was 7.87 g/cm^3. The displacement threshold energy of key elements (Fe and Cr) in the steel was 40 eV [23]. For the sequential irradiation of He and H, the damage dose for H irradiation was equal to that for He irradiation, with values of 0.005, 0.025, and 0.125 dpa, and the concentration ratio of H to He was fixed at approximately 10 in the PR. For the separate irradiation of He and H, the damage dose for both H and He irradiation was 0.125 dpa in the PR. The detailed irradiation parameters are given in Table 1.

2.3 Spherical nanoindentation

All of the irradiated samples were tested using a Nano Indenter G200 in the continuous stiffness measurement (CSM) mode at room temperature. A spherical indenter

Table 1 Detailed parameters for sequential and separate irradiation of He and H

Samples	Ions	Plateau damage (dpa)	Plateau concentration (appm)
1# (He + H)	He^+	0.005	100
	H^+	0.005	1200
2# (He + H)	He^+	0.025	500
	H^+	0.025	5800
3# (He + H)	He^+	0.125	2500
	H^+	0.125	29,000
4# (H)	H^+	0.125	29,000
5# (He)	He^+	0.125	2500

with a radius of 5 μm was used in the tests. The oscillation frequency and amplitude were 45 Hz and 2 nm, respectively. A 2 × 5 indentation array with 70 μm spacing between adjacent indents was created on each specimen to eliminate the influence of the grain orientation. The maximum penetrating depth of the indenter was 2 μm, covering the whole irradiated region (see Fig. 1).

The protocol used in the spherical nanoindentation data analysis (including an effective zero-point correction) was based on Hertz's model [25]. For the frictionless contact between two linear isotropic elastic solids, the effective modulus of the indenter and specimen system, E_{eff}, can be described as follows:

$$\frac{1}{E_{eff}} = \frac{1-v_s^2}{E_s} + \frac{1-v_i^2}{E_i}. \tag{1}$$

Here, v and E refer to Poisson's ratio and Young's modulus, respectively, while subscripts s and i represent the specimen and indenter, respectively. In this test, Poisson's ratios for the specimen (υ_s) and diamond indenter (υ_i) were 0.29 and 0.07, respectively. Young's modulus for the indenter (E_i) was 1140 GPa.

The indentation stress, σ_{ind}, and strain, ε_{ind}, can be defined as follows [13, 16, 26]:

$$\sigma_{ind} = \frac{P}{\pi a^2}, \tag{2}$$

$$\varepsilon_{ind} = \frac{h}{2.4a}. \tag{3}$$

Here, P and h denote the load and displacement, respectively. It is important to note that both P and h have already been zero-point corrected by the method reported in a reference [16]. The contact radius, a, is determined from the CSM stiffness, S, and effective modulus, E_{eff}, in Eq. (4) [16].

$$a = \frac{S}{2E_{eff}} \tag{4}$$

Combined with the above equations, the indentation stress–strain curve can be obtained by converting from the load–displacement curve.

2.4 Microstructure characterization

2.4.1 *Positron annihilation Doppler broadening spectroscopy (DBS)*

Tiny gas-vacancy complexes are invisible under transmission electron microscopy (TEM) because of its limited resolution, but they can be detected by DBS. In this study, DBS measurements were conducted at the Institute of High Energy Physics, Chinese Academy of Science (CAS). The method and detailed procedure of the DBS measurements can be found in our previous report [27].

2.4.2 *TEM*

In order to investigate the microstructural changes induced by irradiation. TEM specimens with a thickness of approximately 70 nm were prepared using a focused ion beam (FIB) system. The microstructure of each specimen was observed using TEM (model FEI Tecnai G2 F20 S-TWIN operated at 200 kV). Specifically, bubble observation was performed under defocus conditions, while dislocation observation was carried out under two-beam conditions with $g = \ <110>$.

3 Results

3.1 Indentation stress–strain response

The spherical indentation stress–strain curves were obtained according to Eqs. (3) and (4), as shown in Figs. 2a and b. The spherical indentation stress–strain relationship of an irradiated sample with a higher damage dose (such as sample #3) could be divided into three segments, including the initial hardening, "strain softening (where the indentation stress decreased with the indentation strain)," and working hardening [28, 29]. In the initial hardening segment, the slope of the linear elastic stage represents the indentation modulus (E_{ind}), which can be calculated to be 183 GPa using Eq. (2), where Young's modulus of the sample (E_s) is approximately 200 GPa, as obtained by the indentation experiments. The yield stress (σ_y) refers to the indentation stress at the beginning of plastic deformation. In the "strain softening" segment, σ_s and σ_e represent the indentation stress at the start and end of the "strain softening", respectively. After σ_e, the indentation stress

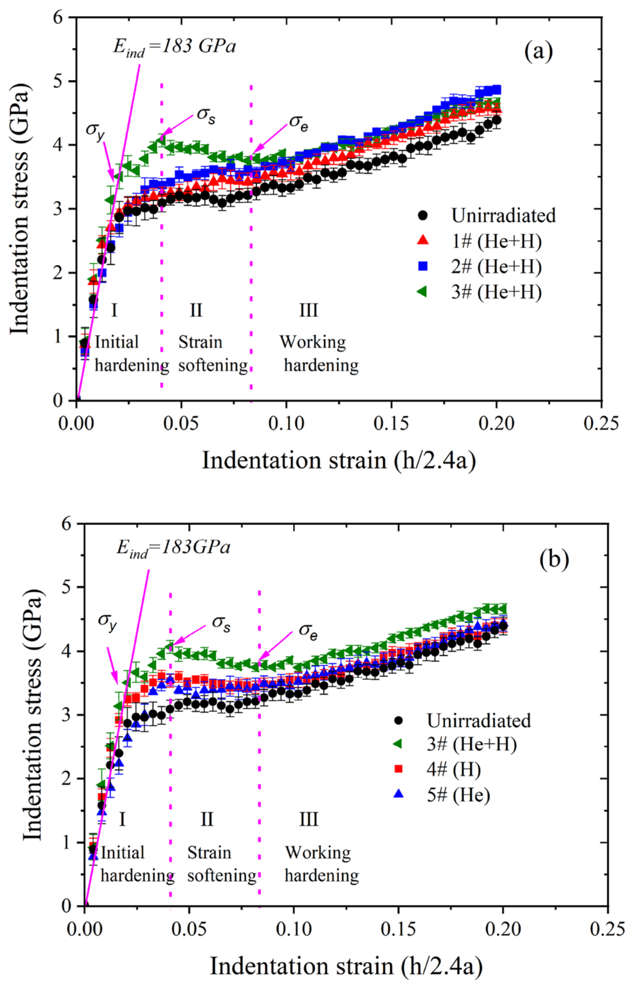

Fig. 2 (Color online) Spherical indentation stress–strain curves of H/He irradiated samples. **a** Dose effect of He and H sequentially irradiated samples. **b** Comparison of the He and H sequentially and separately irradiated samples. The curves can be divided into three segments: (I) the initial hardening segment, (II) "strain softening" segment, and (III) working hardening segment

gradually increases with the strain as a result of the effect of working hardening.

Figure 2a shows the spherical indentation stress–strain curves of the samples sequentially irradiated with He and H at different irradiation doses. The indentation stress values (σ_y, σ_s, and σ_e) for all the samples are given in Table 2. Compared to the unirradiated sample, the yield stress (σ_y) values of samples #1 and #2 hardly changed, but that of sample #3 increased by 1 GPa. Meanwhile, "strain softening" was observed in sample #3. Figure 2b shows a comparison of the spherical indentation stress–strain responses of the samples subjected to sequential and separate irradiation with He and H, when the irradiation doses of both H and He were 0.125 dpa in the PR. Combined with the stress values, σ_s and σ_e, given in Table 2, it shows that the yield stress (σ_y) was greater and the "strain softening" was more remarkable after the sequential He and H irradiation, compared to those for single H/He irradiation.

Table 2 Values of indentation stresses (σ_y, σ_s, and σ_e) for unirradiated and H/He irradiated samples

Samples	σ_y (GPa)	σ_s (GPa)	σ_e (GPa)
Unirradiated	2.7	3.1	3.2
1# (He + H)	2.7	3.2	3.4
2# (He + H)	2.7	3.3	3.6
3# (He + H)	3.5	4.1	3.8
4# (H)	3.2	3.6	3.4
5# (He)	3	3.6	3.4

3.2 Irradiation-induced micro-defects

3.2.1 Vacancy-type defects

In DBS measurements, the concentration and size of vacancy-type defects can be characterized by the *S* parameter because of its sensitivity to low-momentum electrons (that is, valence electrons) around vacancies [30]. In this study, we used the relative change in the *S* parameter after irradiation ($\triangle S/S$) [27] to determine the vacancy-type defects caused by irradiation.

Figure 3a shows the $\triangle S/S$ values versus the depth after the sequential irradiation of He and H at different irradiation doses. When the damage level induced by H/He in the PR increased from 0.005 (sample #1) to 0.025 dpa (sample #2), $\triangle S/S$ showed little change, but when it increased to 0.125 dpa (sample #3), $\triangle S/S$ increased significantly. This revealed that when the damage level was high enough, the formation of vacancy-type defects was more obvious.

Figure 3b shows a comparison of the $\triangle S/S$ values after the sequential (sample #3) and separate irradiation of He and H (samples 4# and #5). In the SR, there was no difference in $\triangle S/S$. However, in the TR and PR, the $\triangle S/S$ value after He and H sequential irradiation (sample #3) was larger than that for single He irradiation (sample #5), but lower than that for single H irradiation (sample #4). This shows that the *S* parameter was influenced by gas atoms (He/H). It has been reported that both He and H prefer to occupy a region with low electronic density, such as a vacancy [31]. Once occupied by He or H, the vacancy will become less effective in the trapping of positrons, resulting in a decrease in the *S* parameter [32–34]. Furthermore, the effect of He on the *S* parameter is more significant than that of H [24, 33, 35]. The preferential occupation of a vacancy by He followed by H (this could suggest the formation of

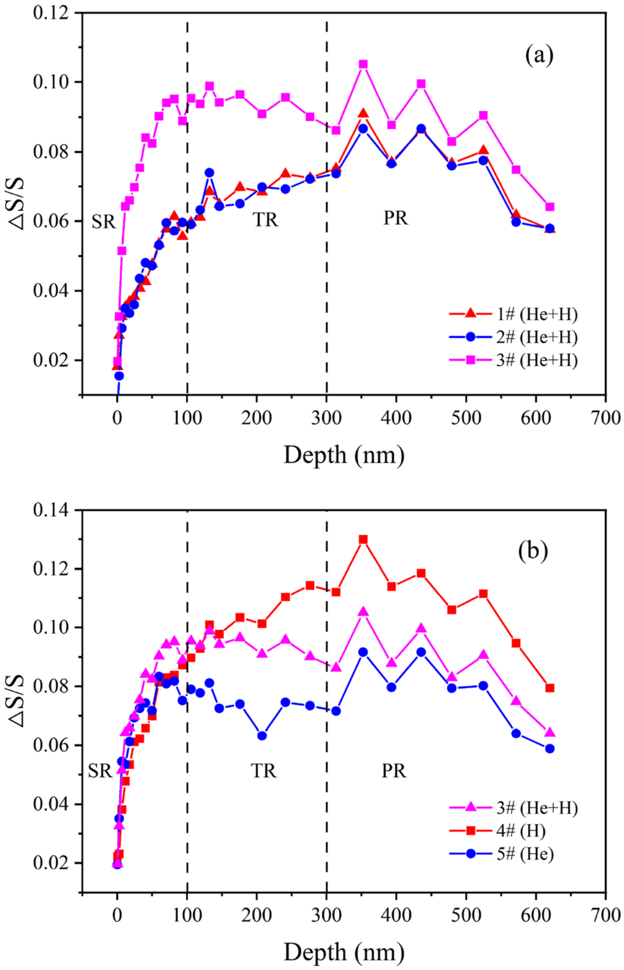

Fig. 3 (Color online) **a** Depth profiles of $\triangle S/S$ after sequential irradiation of He and H at different damage levels induced by H/He (0.005 dpa for sample #1, 0.025 dpa for sample #2, and 0.125 dpa for sample #3) in plateau region. **b** Comparison of $\triangle S/S$ values after He and H sequential irradiation and separate irradiation when the damage level induced by H/He was 0.125 dpa in the plateau region

He-V-H defect clusters) led to a decrease in the *S* parameter after He and H sequential irradiation.

3.2.2 Bubbles

Figure 4 shows the TEM morphology of the bubbles distributed in the PR for H/He irradiated samples obtained using the under-focus condition (approximately 300 nm). It should be noted that visible bubbles were only formed in sample #3, showing the promoted formation of bubbles by the sequential irradiation of He and H.

3.2.3 Dislocation loops

Figure 5 shows that a higher density of black-dots existed in sample #3, compared with samples #4 and #5. Two kinds of dislocation loops are generally formed in Fe-based alloys during irradiation, with Bragger vectors $\boldsymbol{b} = 1/2 < 111 >$ and $\boldsymbol{b} = < 100 >$ [36, 37]. The ratio of $1/2 < 111 >$ to $< 100 >$ loops depends largely on the irradiation temperature and dose [38, 39]. At a low temperature and low dose, irradiation-induced dislocation loops are predominantly small $1/2 < 111 >$ loops formed by a coalescence of self-interstitial atoms (SIAs) [40], appearing as "black-dots" under TEM observation.

4 Discussions

4.1 Spherical nanoindentation stress–strain response

An important phenomenon for materials that have been irradiated with a higher dose (such as sample #3) is an increase in the indentation yield stress, which can be considered to be a manifestation of irradiation hardening [28, 41]. Irradiation hardening in metals or alloys can be described by the Orowan hardening model [42]. According to this model, the irradiation hardening is ascribed to dislocation pinning by irradiation-induced defect clusters. Meanwhile, the change in the uniaxial yield stress ($\Delta\sigma_{uy}$) induced by irradiation can be quantified by the following equation:

$$\Delta\sigma_{uy} = M\sigma\mu b\sqrt{Nd}, \quad (5)$$

where M is the Taylor factor (approximately 0.36); σ represents the strength factor of the specific barrier for dislocation slipping (0.2 for black dots, 0.1 for voids or bubbles, 0.2 for dislocation lines) [42]; u is the shear modulus of the material (80 GPa for bcc-Fe); b is the Burgers vector (0.248 nm for $1/2 < 111 >$ dislocation loops in bcc-Fe) [43]; and N and d refer to the density and mean diameter of the specific barrier, respectively.

Based on TEM observations, the densities and mean diameters of the bubbles and black dots in the H/He irradiated samples are given in Table 3. Correspondingly, the increase in the uniaxial yield strength (σ_{uy}) can be calculated by Eq. (6). It has been shown that the indentation yield strength is approximately double the uniaxial yield strength (σ_{uy}) [20, 44, 45]. Accordingly, the increase in the indentation yield strength can be converted to that of the uniaxial yield strength. A comparison of the uniaxial yield strength from the Orowan hardening model with that from the spherical indentation showed that the former was lower than the latter. This discrepancy was attributed to the indentation size effect (ISE). For spherical indenters, the ISE is more significantly dependent on the indenter size rather than the indentation depth [46, 47]. In particular, as the radius of the sphere decreases, the hardness increases.

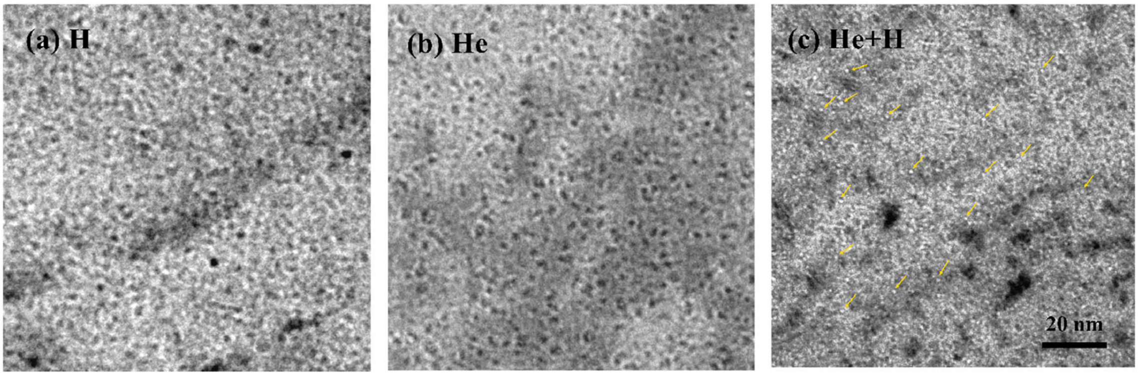

Fig. 4 TEM morphology of bubbles distributed in PR for H (sample #4), He (sample #5), and He + H (sample #3) samples. Photographs were taken in the bright-field under-focus (approximately 300 nm) mode

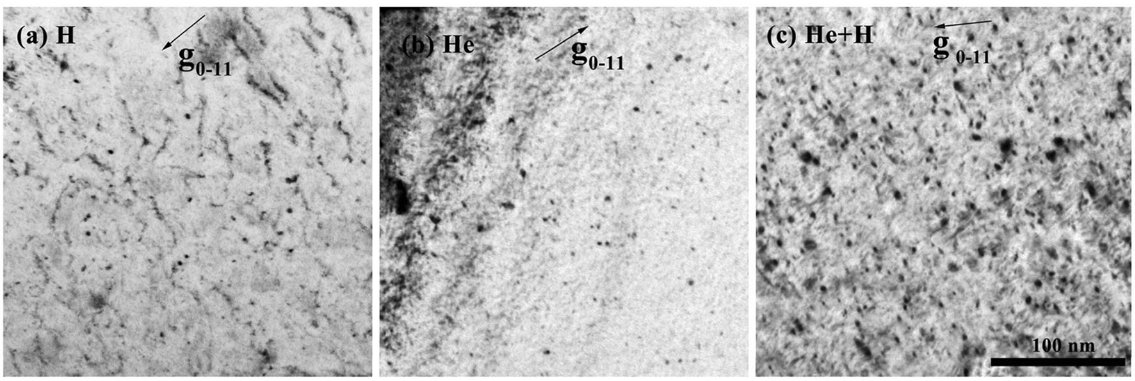

Fig. 5 TEM morphology of small interstitial dislocation loops (black dots) distributed in PR for H (sample #4), He (sample #5), and He + H (sample #3) samples. Photographs were taken under two-beam conditions with g = (0–11)

Table 3 Densities and mean diameters of bubbles and black dots in H/He irradiated samples, and corresponding increase in yield strength obtained by Orowan hardening model, in comparison with that from spherical indentation test

Samples	Bubbles		Black dots		$\Delta\sigma_{uy}$	
	Diameter (nm)	Density (10^{23}/m^3)	Diameter (nm)	Density (10^{22}/m^3)	From indentation (GPa)	From Orowan model (GPa)
3# (He + H)	0.64 ± 0.04	5.86 ± 0.29	3.00 ± 0.15	8.32 ± 0.30	0.4	0.31
4# (H)	–	–	2.65 ± 0.29	5.00 ± 0.41	0.25	0.14
5# (He)	–	–	2.58 ± 0.10	3.58 ± 0.19	0.15	0.12

For indenter radii of 100 µm and less, the indentation stress–strain curves shift upward with the decreasing radii and deviate measurably from the macroscopic stress–strain behavior [46]. In this study, the radius of the spherical indenter was 5 µm (less than 100 µm). Therefore, the yield stress from indentation was higher than the uniaxial yield strength from the uniaxial tensile test or Orowan model.

Another phenomenon is the appearance of "strain-softening" after the yield point. This "strain-softening" is not related to the material deformation or hardening behavior, but is largely attributable to the softening effect induced by the substrate [17, 28, 29]. The effect of a softer substrate is related to the size of the plasticity affected region (PAR). The volume of the PAR can be calculated as follows [48]:

$$V = 2/3\pi(R_{\mathrm{PAR}})^3, \tag{6}$$

where R_{PAR} refers to the radius of the plastic zone, which can be approximated by $R_{\mathrm{PAR}} \approx fa$, where f is the proportional coefficient.

The indentation stress increased with the strain before reaching the indentation stress at the onset of "strain-softening" (σ_s). In the meantime, the PAR did not exceed the damage layer. As the PAR extended toward the softer substrate beneath the damage layer, the hardness appeared to decrease. Figure 2 shows that the indentation strain at the onset of "strain-softening" was 0.04, and the corresponding contact radius was 498 nm, as calculated by Eq. (4). According to the suggestion by Chioct et al. that $f = 1.44$ [49], the radius of PAR (R_{PAR}) could be calculated to be 717 nm. This value was approximately equal to the maximum depth of the damage region obtained by SRIM calculations.

The appearance of "strain-softening" is also associated with the ISE [46–48, 50]. On one hand, the hardness decreases with the increasing penetration depth of the indenter (i.e., the indenter radius) in the initial hardening segment. On the other hand, for smaller indenter radii, the ISE shifts the indentation stress–strain curves upward [46], resulting in a higher indentation yield stress and critical indentation stress at the onset of "strain-softening" (σ_s).

4.2 H/He synergistic effects on mechanical properties

Compared to single He/H irradiation, a higher indentation yield stress was observed after He and H sequential irradiation, indicating that enhanced hardening had occurred as a result of the He and H irradiation. Based on triple-beam (Fe + He + H) irradiation experiments, Lee and Hunn et al. reported similar effects in *F/M* steels and stainless steels [7, 9]. They considered that the enhancement of the hardening by the synergy of H and He was due to the dislocation pinning by bubbles and dislocation loops. The production of dislocation loops resulted from the punching of over-pressurized bubbles or an accumulation of surplus SIAs left over during the formation of gas-vacancy clusters. They also speculated that the reason was related to the trapping of hydrogen by helium clusters. The present study confirmed that the formation of both bubbles and dislocation loops was enhanced by the synergy of He and H irradiation.

An atomistic simulation indicated that the trapping of hydrogen by helium bubbles is more beneficial for the production of dislocation loops by the "loop punching" of He bubbles [6]. More specifically, there are two kinds of primary crystal defects, namely vacancies and SIAs (Frank pairs), produced in the early stages of an irradiation event. At room temperature, the formation of defect-clusters is primarily determined by the fate of SIAs because of their higher mobility compared to vacancies [51]. A migrating interstitial atom could encounter a vacancy and they could annihilate each other, or it could encounter other interstitial atoms and form interstitial clusters and dislocation loops, or it could be absorbed by a defect sink (such as a grain boundary, precipitate, or dislocation). However, these processes are influenced by transmutation gas atoms (H/He). He can easily be trapped by vacancies, forming stabilized He-vacancy complexes, and leading to the decreased possibility of SIAs recombining with these vacancies. When the concentration of He aggregated in the vacancy clusters is high enough, the lattice atoms around the vacancy clusters will be emitted into the bulk as new SIAs or absorbed by interstitial dislocation loops, accompanied by the growth of bubbles. Furthermore, some studies [6, 31, 52] have shown that a He-vacancy cluster (or He bubble) is a strong trap for H. The binding of H and He-vacancy clusters is more favorable for vacancy-interstitial pair production. This means that the co-presence of H and He can lead to a lower possibility of SIAs recombining with vacancies and a stronger "loop punching" effect.

Compared to triple-beam irradiation, double-beam (He + H) irradiation at room temperature is closer to the special condition of a continuous helium but insufficient vacancy supply because of higher gas/dpa rates [53]. Therefore, it can be inferred that "loop punching" might have been a vital mechanism for the nucleation or growth of both the bubbles and dislocation loops in sample #3. In addition, a higher H to He concentration ratio (10:1) suggests that the contribution of H to "loop punching" was more outstanding because of the trapping of H by He bubbles.

In summary, the co-presence of H and He was more beneficial for the nucleation and growth of vacancy-type (bubbles or voids) and interstitial-type defect clusters (I-loops), resulting in more severe hardening.

5 Conclusion

This study investigated the synergistic effect of He and H irradiation on the mechanical properties of SIMP steel using spherical nanoindentation. In addition, the intrinsic mechanism of the induced changes was investigated using DBS and TEM. It was found that the sequential irradiation of He and H with higher irradiation doses resulted in an increase in the indentation yield stress and the appearance of "strain softening." This reflected the presence of an irradiation-induced hardening layer. More importantly, the indentation yield stress after the sequential irradiation of He and H was greater than that after separate irradiation, which was ascribed to the enhanced formation of vacancy-type (such as bubbles) and interstitial-type (such as I-loops) defect clusters by the synergistic effect of H and He irradiation.

Acknowledgements The authors would like to express their sincere gratitude to all their colleagues from the laboratory of nuclear engineering materials and the staff of the Heavy Ion Research Facility at Lanzhou (HIRFL), Low Energy Accelerator Facility (LEAF) and 320 kV multi-discipline research platform (320 kV). In addition, they thank Professor Qiu-Lin Li, master Hao Wu, and Dr. Liang Wang for their support with the spherical indentation tests. The authors also thank Mrs. Hui-Ping Liu for her TEM support.

Author contributions All authors contributed to the study conception and design. Material preparation, data collection and analysis were performed by Peng Jin, Tie-Long Shen, Jing Li and Yu-Shan Yang. The first draft of the manuscript was written by Peng Jin and all authors commented on previous versions of the manuscript. All authors read and approved the final manuscript.

References

1. J. Marian, T. Hoang, M. Fluss et al., A review of helium–hydrogen synergistic effects in radiation damage observed in fusion energy steels and an interaction model to guide future understanding. J. Nucl. Mater. **462**, 409–421 (2015). https://doi.org/10.1016/j.jnucmat.2014.12.046
2. S.J. Zinkle, L.L. Snead, Designing radiation resistance in materials for fusion energy. Annu. Rev. Mater. Res. **44**, 241–267 (2014). https://doi.org/10.1146/annurev-matsci-070813-113627
3. P. Vladimirov, A. Möslang, Irradiation conditions of ADS beam window and implications for window material. J. Nucl. Mater. **356**, 287–299 (2006). https://doi.org/10.1016/j.jnucmat.2006.05.037
4. T. Tanaka, K. Oka, S. Ohnuki et al., Synergistic effect of helium and hydrogen for defect evolution under multi-ion irradiation of Fe–Cr ferritic alloys. J. Nucl. Mater. **329–333**, 294–298 (2004). https://doi.org/10.1016/j.jnucmat.2004.04.051
5. E. Wakai, K. Kikuchi, S. Yamamoto et al., Swelling behavior of F82H steel irradiated by triple/dual ion beams. J. Nucl. Mater. **318**, 267–273 (2003). https://doi.org/10.1016/s0022-3115(03)00122-3
6. E. Hayward, C. Deo, Synergistic effects in hydrogen-helium bubbles. J. Phys. Condens. Matter **24**, 265402 (2012). https://doi.org/10.1088/0953-8984/24/26/265402
7. E.H. Lee, J.D. Hunn, G.R. Rao et al., Triple ion beam studies of radiation damage in 9Cr-2WVTa ferritic/martensitic steel for a high power spallation neutron source. J. Nucl. Mater. **271–272**, 385–390 (1999). https://doi.org/10.1016/s0022-3115(98)00722-3
8. E. Wakai, M. Ando, T. Sawai et al., Effect of gas atoms and displacement damage on mechanical properties and microstructures of F82H. J. Nucl. Mater. **356**, 95–104 (2006). https://doi.org/10.1016/j.jnucmat.2006.05.032
9. J.D. Hunn, E.H. Lee, T.S. Byun et al., Helium and hydrogen induced hardening in 316LN stainless steel. J. Nucl. Mater. **282**, 131–136 (2000). https://doi.org/10.1016/s0022-3115(00)00424-4
10. W.C. Oliver, G.M. Pharr, Measurement of hardness and elastic modulus by instrumented indentation: advances in understanding and refinements to methodology. J. Mater. Res. **19**, 3–20 (2011). https://doi.org/10.1557/jmr.2004.19.1.3
11. P. Hosemann, Small-scale mechanical testing on nuclear materials: bridging the experimental length-scale gap. Scr. Mater. **143**, 161–168 (2018). https://doi.org/10.1016/j.scriptamat.2017.04.026
12. Y. Yang, C. Zhang, Y. Meng et al., Nanoindentation on V–4Ti alloy irradiated by H and He ions. J. Nucl. Mater. **459**, 1–4 (2015). https://doi.org/10.1016/j.jnucmat.2015.01.020
13. S. Pathak, S.R. Kalidindi, Spherical nanoindentation stress–strain curves. Mater. Sci. Eng. **91**(1), 36 (2015). https://doi.org/10.1016/j.mser.2015.02.001
14. C.D. Hardie, S.G. Roberts, A.J. Bushby, Understanding the effects of ion irradiation using nanoindentation techniques. J. Nucl. Mater. **462**, 391–401 (2015). https://doi.org/10.1016/j.jnucmat.2014.11.066
15. D.E.J. Armstrong, C.D. Hardie, J.S.K.L. Gibson et al., Small-scale characterisation of irradiated nuclear materials: part II nanoindentation and micro-cantilever testing of ion irradiated nuclear materials. J. Nucl. Mater. **462**, 374–381 (2015). https://doi.org/10.1016/j.jnucmat.2015.01.053
16. S.R. Kalidindi, S. Pathak, Determination of the effective zero-point and the extraction of spherical nanoindentation stress–strain curves. Acta Mater. **56**, 3523–3532 (2008). https://doi.org/10.1016/j.actamat.2008.03.036
17. C.D. Hardie, S.G. Roberts, A.J. Bushby, Mechanical behavior of ion-irradiated Fe-Cr alloys investigated by spherical indentation. Mater. Res. Soc. Symp. Proc. (2012). https://doi.org/10.1557/opl.2012
18. A.J. Bushby, S.G. Roberts, C.D. Hardie, Nanoindentation investigation of ion-irradiated Fe–Cr alloys using spherical indenters. J. Mater. Res. **27**, 85–90 (2011). https://doi.org/10.1557/jmr.2011.304
19. S. Pathak, S.R. Kalidindi, J.S. Weaver et al., Probing nanoscale damage gradients in ion-irradiated metals using spherical nanoindentation. Sci. Rep. **7**, 11918 (2017). https://doi.org/10.1038/s41598-017-12071-6
20. J.S. Weaver, C. Sun, Y. Wang et al., Quantifying the mechanical effects of He, W and He + W ion irradiation on tungsten with spherical nanoindentation. J. Mater. Sci. **53**, 5296–5316 (2017). https://doi.org/10.1007/s10853-017-1833-8
21. K. Yang, W. Yan, G.Z. Wang et al., Development of a novel structural material (SIMP steel) for nuclear equipment with balanced resistances to high temperature, radiation and liquid metal corrosion. Acta Metall. Sin. **52**, 1207–1221 (2016). https://doi.org/10.11900/0412.1961.2016.00320(inChinese)
22. J.F. Ziegler, M.D. Ziegler, J.P. Biersack, SRIM – The stopping and range of ions in matter (2010). Nucl. Instrum. Methods Phys. Res Sect. B. **268**, 1818–1823 (2010). https://doi.org/10.1016/j.nimb.2010.02.091
23. R.E. Stoller, M.B. Toloczko, G.S. Was et al., On the use of SRIM for computing radiation damage exposure. Nucl. Instrum. Methods Phys. Res. Sect. B **310**, 75–80 (2013). https://doi.org/10.1016/j.nimb.2013.05.008
24. J. Qiu, X. Ju, Y. Xin et al., He and H-implanted CLAM steel investigated by positron-annihilation spectroscopy. J. Nucl. Mater. **411**, 20–24 (2011). https://doi.org/10.1016/j.jnucmat.2011.01.022
25. H. Hertz, *Miscellaneous Papers* (Macmillan and co.Collection, New York, 1896), p. 384
26. D. Tabor, *The Hardness of Metals* (UK Clarendon Press, Oxford, 1951)
27. P. Jin, T. Shen, M. Cui et al., Study on vacancy-type defects in SIMP steel induced by separate and sequential H and He ion implantation. J. Nucl. Mater. **520**, 131–139 (2019). https://doi.org/10.1016/j.jnucmat.2019.04.012
28. W.Q. Chen, X.Y. Wang, X.Z. Xiao et al., Characterization of dose dependent mechanical properties in helium implanted tungsten. J. Nucl. Mater. **509**, 260–266 (2018). https://doi.org/10.1016/j.jnucmat.2018.07.004
29. X. Xiao, D. Terentyev, L. Yu, Model for the spherical indentation stress-strain relationships of ion-irradiated materials. J. Mech. Phys. Solids **132**, 103694 (2019). https://doi.org/10.1016/j.jmps.2019.103694
30. M. Eldrup, Positron methods for the study of defects in bulk materials. J. Phys. **05**(C1), C1-93-C1-103 (1995). https://doi.org/10.1051/jp4:1995111

31. C.J. Ortiz, R. Vila, J.M. Pruneda, Ab initio study of helium and hydrogen interactions in α -Fe. Physics, 1–5 (2012).
32. T. Troev, E. Popov, P. Staikov et al., Positron lifetime studies of defects in α-Fe containing helium. Phys. Status Solidi C **6**, 2373–2375 (2009). https://doi.org/10.1002/pssc.200982129
33. T. Troev, A. Markovski, S. Peneva et al., Positron lifetime calculations of defects in chromium containing hydrogen or helium. J. Nucl. Mater. **359**, 93–101 (2006). https://doi.org/10.1016/j.jnucmat.2006.07.020
34. Q. Xu, E. Popov, T. Troev et al., Positron lifetime calculation of vacancy clusters in tantalum containing hydrogen and helium. J. Nucl. Mater. **506**, 71–75 (2018). https://doi.org/10.1016/j.jnucmat.2017.06.011
35. T. Zhu, B. Wang, L. Song et al., Sensitivity of positrons at hydrogen storage sites in FeCr alloy containing vacancy and helium atom. Int. J. Hydrog. Energy **45**, 15571–15577 (2020). https://doi.org/10.1016/j.ijhydene.2020.04.025
36. S. Xu, Z. Yao, M.L. Jenkins, TEM characterisation of heavy-ion irradiation damage in FeCr alloys. J. Nucl. Mater. **386–388**, 161–164 (2009). https://doi.org/10.1016/j.jnucmat.2008.12.078
37. S.J. Zinkle, B.N. Singh, Microstructure of neutron-irradiated iron before and after tensile deformation. J. Nucl. Mater. **351**, 269–284 (2006). https://doi.org/10.1016/j.jnucmat.2006.02.031
38. J. Chen, P. Jung, W. Hoffelner et al., Dislocation loops and bubbles in oxide dispersion strengthened ferritic steel after helium implantation under stress. Acta Mater. **56**, 250–258 (2008). https://doi.org/10.1016/j.actamat.2007.09.016
39. B. Yao, D.J. Edwards, R.J. Kurtz, TEM characterization of dislocation loops in irradiated bcc Fe-based steels. J. Nucl. Mater. **434**, 402–410 (2013). https://doi.org/10.1016/j.jnucmat.2012.12.002
40. J. Marian, B.D. Wirth, J.M. Perlado, Mechanism of formation and growth of <100> interstitial loops in ferritic materials. Phys. Rev. Lett. **88**, 255507 (2002). https://doi.org/10.1103/PhysRevLett.88.255507
41. J.T. Busby, M.C. Hash, G.S. Was, The relationship between hardness and yield stress in irradiated austenitic and ferritic steels. J. Nucl. Mater. **336**, 267–278 (2005). https://doi.org/10.1016/j.jnucmat.2004.09.024
42. G.S. Was, *Fundamentals of Radiation Materials Science, Metals and Alloys*, 2nd edn. (Springer, New York, 2017), pp. 682–696
43. B. Li, Z. Wang, K. Wei et al., Evaluation of helium effect on irradiation hardening in F82H, ODS, SIMP and T91 steels by nano-indentation method. Fusion Eng. Des. **142**, 6–12 (2019). https://doi.org/10.1016/j.fusengdes.2019.04.049
44. D.K. Patel, S.R. Kalidindi, Correlation of spherical nanoindentation stress-strain curves to simple compression stress-strain curves for elastic-plastic isotropic materials using finite element models. Acta Mater. **112**, 295–302 (2016). https://doi.org/10.1016/j.actamat.2016.04.034
45. J.S. Weaver, S.R. Kalidindi, Mechanical characterization of Ti-6Al-4V titanium alloy at multiple length scales using spherical indentation stress-strain measurements. Mater. Des. **111**, 463–472 (2016). https://doi.org/10.1016/j.matdes.2016.09.016
46. G.M. Pharr, E.G. Herbert, Y. Gao, The indentation size effect: a critical examination of experimental observations and mechanistic interpretations. Annu. Rev. Mater. Res. **40**, 271–292 (2010). https://doi.org/10.1146/annurev-matsci-070909-104456
47. I.J. Spary, A.J. Bushby, N.M. Jennett, On the indentation size effect in spherical indentation. Philos. Mag. **86**, 5581–5593 (2006). https://doi.org/10.1080/14786430600854988
48. K. Durst, M. Göken, G.M. Pharr, Indentation size effect in spherical and pyramidal indentations. J. Phys. D Appl. Phys. **41**, 074005 (2008). https://doi.org/10.1088/0022-3727/41/7/074005
49. D. Chicot, Hardness length-scale factor to model nano- and micro-indentation size effects. Mater. Sci. Eng. A **499**, 454–461 (2009). https://doi.org/10.1016/j.msea.2008.09.040
50. P. Haušild, Methodological comment on the nanoindentation of ion-irradiation hardened materials. J. Nucl. Mater. **551**, 152987 (2021). https://doi.org/10.1016/j.jnucmat.2021.152987
51. R. Smith, L. Malerba, D.J. Bacon et al., State-of-the-Art Report on Structural Materials. (Nuclear Science NEA/NSC/R, OECD, 2017), p. 25
52. H. Zhou, Y. Liu, S. Jin et al., Towards suppressing H blistering by investigating the physical origin of the H-He interaction in W. Nucl. Fusion **50**, 115010 (2010). https://doi.org/10.1088/0029-5515/50/11/115010
53. N. Gao, H. Van Swygenhoven, M. Victoria et al., Formation of dislocation loops during He clustering in bcc Fe. J. Phys. Condens. Matter **23**, 442201 (2011). https://doi.org/10.1088/0953-8984/23/44/442201